

Resonance properties of tidal channels with multiple retention basins: role of adjacent sea

Pieter C. Roos · Henk M. Schuttelaars

Received: 29 August 2014 / Accepted: 15 January 2015 / Published online: 12 February 2015
© The Author(s) 2015. This article is published with open access at Springerlink.com

Abstract We present an idealised model of the tidal response in a main channel with multiple secondary basins, co-oscillating with an adjacent sea. The sea is represented as a semi-infinite strip of finite width, anywhere between the limits of a channel extension (narrow) and a half-plane (wide). The sea geometry controls the extent to which radiative damping takes place and hence the type of conditions that effectively apply at the channel mouth. These conditions range between the two extremes of prescribing elevation (deep sea limit) and prescribing the incoming wave (sea as channel extension of the same depth, as done in an earlier study). The closer to this first extreme, the stronger the oscillations in the secondary basins may feed back onto the channel mouth and thus produce an amplified or weakened response in the system as a whole. The possibly resonant response is explained by analysing the additional waves that emerge on either side of the entrance of the secondary basin. Finally, we show that the simultaneous presence of two secondary basins may amplify or weaken the accumulated responses to these basins individually.

Keywords Tidal channel · Retention basins · Resonance · Radiative damping · Idealised process-based modelling

Responsible Editor: Emil Vassilev Stanev

P. C. Roos (✉)
Water Engineering and Management, University of Twente, P.O.
Box 217, 7500 AE Enschede, The Netherlands
e-mail: p.c.roos@utwente.nl

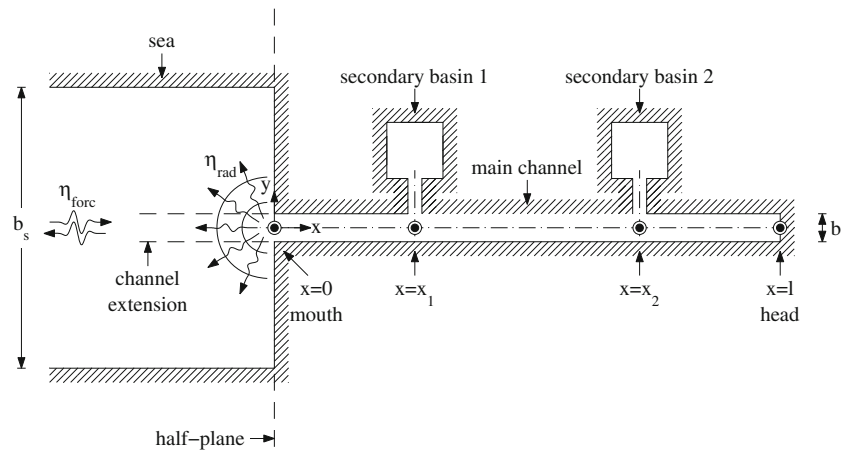
H. M. Schuttelaars
Delft Institute of Applied Mathematics, Delft University
of Technology, P.O. Box 5031, 2600 GA Delft, The Netherlands

1 Introduction

Recent studies have shown that the construction of retention basins may influence the tidal motion in estuaries. Such measures are considered, e.g., to reduce both high waters and turbidity (Ems Estuary, see Donner et al. 2012) or to achieve nature compensation (de-poldering to compensate for the loss of natural values associated with the deepening of the Western Scheldt, see Stronkhorst and Mulder 2014). Alebregtse et al. (2013) showed that the response at the channel head to a single secondary basin depends on its distance δ to the channel head relative to the tidal wavelength λ . An alternating pattern is found: reduction occurs if $\delta < \frac{1}{4}\lambda$, amplification if $\frac{1}{4}\lambda < \delta < \frac{1}{2}\lambda$, reduction again if $\frac{1}{2}\lambda < \delta < \frac{3}{4}\lambda$, and so on. Maximum reduction or maximum amplification is found halfway along these intervals. It should be emphasized that this result applies to the case without friction. Moreover, the secondary basins are represented as short linear channels that are small in the sense that the combined effect of multiple retention basins is a linear superposition of the individual effects of each basin separately. In a nonlinear follow-up study, Alebregtse and de Swart (2014) found that quadratic friction produces spatial variations in tidal range landward of the secondary channel. Moreover, the effects on suspended sediment transport are stronger (net transport may locally reverse) than those on bedload transport.

However, the conditions applied at the channel mouth deserve attention here, particularly regarding the concept of resonance, which implies high values of the ratio of elevation amplitude at the channel head and the amplitude of the wave that forces the problem. By imposing

Fig. 1 Top view of model geometry, showing a main channel of length l and width b , connected to a sea of width b_s infinitely stretching to the left. Dashed lines denote the coastlines in the two limiting cases of a half-plane ($b_s \rightarrow \infty$) and a channel extension ($b_s = b$). This is an example with two secondary Helmholtz basins ($J = 2$) at $x = x_1$ and $x = x_2$. Black circles indicate the channel mouth, the vertex points and the channel head



the incoming tidal wave, the above studies rule out the possibility of resonance of the system as a whole and thus also neglect the potential influence of the secondary basin on these resonance properties. In other words, interference of the ingoing and outgoing wave at the main channel cannot affect the response in the system. This assumption implies that the channel is effectively treated as being infinitely long. Indeed, the results were found to depend on the distance from secondary basin to channel head only and not on the distance to channel mouth (and hence on channel length).

The goal of this study is to investigate the resonance properties of the main channel with multiple secondary basins. As the main innovation, we specifically focus on the forcing of the system and thus on the interaction of the basin with the adjacent sea. Sea geometry is crucial herein, because it controls the amount of water available to absorb the wave radiating away from the channel mouth. As shown in Fig. 1, the widest possibility is a half-plane, the narrowest an extension of the main channel, as effectively considered by Alebregtse et al. (2013). To connect these two limiting cases, we will in fact consider the intermediate configuration where the sea is represented as a semi-infinite strip of finite width b_s . Importantly, the forcing wave mentioned above when characterising resonance is in the sea and not in the main channel. A further innovation is that a broader range of basin characteristics will be systematically analysed, regarding both single basin response and the interaction among basins. This range includes basins that are not small and basins that turn out to display opposite behaviour (i.e. reversed patterns of amplification and reduction).

This paper is organised as follows. Section 2 contains the model formulation. Section 3 is the solution method. Next, the results for one and two secondary basins are presented in Section 4. Finally, Sections 5 and 6 contain the discussion (including an explanation of the physical mechanism) and conclusions, respectively.

2 Model formulation

Consider a straight tidal channel of length l , uniform width b and uniform depth h were connected to a sea and a number of secondary basins (the case with two basins is sketched in Fig. 1). We adopt a two-dimensional coordinate system with horizontal coordinates x and y . The x -coordinate is aligned with the main channel, with the mouth located at $x = 0$ and its head at $x = l$. The y -coordinate follows the coastline of the adjacent sea, with the channel mouth located between $y = \pm \frac{1}{2}b$.

Regarding hydrodynamics, our model combines two approaches. A cross-sectionally averaged approach suffices for the main channel and secondary basins. However, to adequately describe the wave radiating from channel mouth into the sea, we must adopt a two-dimensional approach describing depth-averaged flow and variations in two horizontal directions. The cross-sectionally averaged flow velocity and surface elevation in the main channel are denoted $u(x, t)$ and $\eta(x, t)$, respectively. Conservation of momentum and mass in the main channel is expressed by the cross-sectionally averaged linear shallow water equations

$$\frac{\partial u}{\partial t} + \frac{ru}{h} = -g \frac{\partial \eta}{\partial x}, \quad \frac{\partial \eta}{\partial t} + h \frac{\partial u}{\partial x} = 0, \tag{1}$$

where g is the acceleration of gravity. Moreover, r is a bottom friction coefficient, as specified according to Lorentz' linearisation (Lorentz 1922; Zimmerman 1982) in Appendix A. As boundary conditions for the main channel, we require its elevation and volume transport at the mouth ($x = 0$) to match those in the adjacent sea, as well as no flow at the closed end ($x = l$):

$$\eta = \langle \eta_s \rangle \text{ and } bh u = bh_s \langle u_s \rangle \quad \text{at } x = 0, \tag{2}$$

$$u = 0 \quad \text{at } x = l. \tag{3}$$

Angle brackets denote averaging over the seaward side of the main channel mouth, i.e. $\langle \cdot \rangle = b^{-1} \int_{-b/2}^{b/2} dy$. Equation 2 thus connects the two-dimensional flow

approach in the sea with the cross-sectionally averaged description in the main channel.

The adjacent sea, of uniform depth h_s , is represented as a semi-infinite strip of width b_s , which becomes a half-plane in the limit $b_s \rightarrow \infty$ and a channel extension if $b_s = b$. The solution in the sea satisfies the two-dimensional linearised shallow water equations including bottom friction (Appendix B). It is the superposition of a (partially) standing wave η_{forc} that forces the system and a radiating wave η_{rad} , both of angular frequency ω (see Fig. 1). The former wave, which has a prescribed amplitude N_{forc} at $x = 0$, can be viewed as the superposition of a normally incident wave and a reflected wave as if the channel mouth were closed. The radiating wave, which radiates away from the channel mouth, actually results from the interaction with the channel system and is therefore an unknown of the problem. The elevation in the sea can thus be written as

$$\eta_s = \eta_{\text{forc}} + \eta_{\text{rad}}, \tag{4}$$

with

$$\eta_{\text{forc}} = N_{\text{forc}} \Re \{ \cos(k_s x) \exp(i\omega t) \}, \tag{5}$$

where $k_s = \gamma_s k_{s0}$ is the (complex) wave number in the sea, with frictional correction factor $\gamma_s = \sqrt{1 - i r_s / (\omega h_s)}$ and frictionless shallow water wave number $k_{s0} = \omega / \sqrt{g h_s}$.

Next, we consider J secondary basins, the j -th one located at $x = x_j$. Each secondary basin is represented as a Helmholtz basin, which is motivated by its relatively simple description and the agreement with the plans in practise (such as for the Ems estuary in Northern Germany; see Donner et al. 2012). Helmholtz basins are characterised by the dimensions of a short inlet channel (length l_j , width b_j , depth h_j) and the surface area A_j of the basin. The unknowns are the channel velocity $v_j(t)$, measured positive when pointing towards the basin, and the basin level $\beta_j(t)$, which is assumed uniform, relative to its still water level. The model equations for these scalar quantities read

$$\frac{dv_j}{dt} + \frac{r_j v_j}{h_j} = -g \frac{\beta_j - \eta_j}{l_j}, \quad A_j \frac{d\beta_j}{dt} = b_j h_j v_j, \tag{6}$$

where r_j is a friction coefficient (see Appendix A) and η_j is the surface elevation in the main channel at $x = x_j$. The possibility of considering alternative secondary basin types, such as linear channels, will be discussed in Section 5.3.

The formulation in Eq. 6, assuming a linearly sloping surface elevation in the inlet channel, guarantees continuity of elevation at each of the J vertex points. At those locations, we must further require continuity of volume transports according to

$$bh \left[u_j^\ominus - u_j^\oplus \right] = b_j h_j v_j \text{ at } x = x_j, \tag{7}$$

where superscripts \ominus and \oplus denote the limits to the left and right of $x = x_j$, respectively.

3 Solution method

We seek solutions in dynamic equilibrium with the periodic forcing of angular frequency ω . For the main channel, we thus write

$$\eta(x, t) = \Re \{ N(x) \exp(i\omega t) \}, \tag{8}$$

$$u(x, t) = \Re \{ U(x) \exp(i\omega t) \}, \tag{9}$$

with complex amplitudes $N(x)$ and $U(x)$. For the Helmholtz basins, we let V_j denote the complex amplitude of the inlet channel velocity.

To proceed, let us define the following $J + 2$ complex elevation amplitudes

$$N = [\underbrace{N_0}_{\text{mouth}}, \underbrace{N_1, N_2, \dots, N_J}_{\text{vertex points}}, \underbrace{N_{J+1}}_{\text{head}}]^T, \tag{10}$$

referring to the channel mouth, vertex points and channel head (black dots in Fig. 1). The solution will now be obtained by deriving a set of linear equations for these $J + 2$ unknowns. To this end, we first seek a solution in the main channel, that attains these yet unknown elevation amplitudes N_j while satisfying the model equations for the main channel in Eq. 1. These equations can be combined into a single equation for $N(x)$:

$$\frac{d^2 N}{dx^2} + k^2 N = 0. \tag{11}$$

Here, $k = \gamma k_0$ is the wave number in the main channel (complex due to bottom friction), with frictional correction factor $\gamma = \sqrt{1 - i r / (\omega h)}$ and frictionless shallow water wave number $k_0 = \omega / \sqrt{g h}$. The solution to Eq. 11 is a superposition of waves travelling in opposite directions, i.e. $N(x) = \hat{A} \exp(ikx) + \hat{B} \exp(-ikx)$, i.e. a partially standing wave with coefficients \hat{A} and \hat{B} . In each of the $J + 1$ main channel sections $x_j < x < x_{j+1}$, with for notational convenience $x_0 = 0$ (mouth) and $x_{J+1} = l$ (head), this can be written as

$$N(x) = N_{j+1} \frac{\sin(k[x - x_j])}{\sin(k[x_{j+1} - x_j])} - N_j \frac{\sin(k[x - x_{j+1}])}{\sin(k[x_{j+1} - x_j])}, \tag{12}$$

$$U(x) = \frac{i}{\gamma} \sqrt{\frac{g}{h}} \left[N_{j+1} \frac{\cos(k[x - x_j])}{\sin(k[x_{j+1} - x_j])} - N_j \frac{\cos(k[x - x_{j+1}])}{\sin(k[x_{j+1} - x_j])} \right]. \tag{13}$$

The velocities follow from $i\omega \gamma^2 U = -g dN/dx$. This solution automatically satisfies $N(x_j) = N_j$ and, hence, continuity of surface elevation at each of the vertex points. To also satisfy the remaining conditions in Eqs. 2, 3, and 7, we must turn to the volume transports on either side of each vertex point.

To this end, let U_j^\ominus and U_j^\oplus represent the left and right limits of the complex velocity amplitudes at the points $x =$

x_j , respectively, if they exist in the channel.¹ From Eq. 13, we now find

$$bhU_j^\oplus = \frac{i\omega b}{k} \left[\frac{N_{j+1}}{\sin \varphi_j^\oplus} - \frac{N_j}{\tan \varphi_j^\oplus} \right], \tag{14}$$

$$bhU_j^\ominus = \frac{i\omega b}{k} \left[\frac{N_j}{\tan \varphi_j^\ominus} - \frac{N_{j-1}}{\sin \varphi_j^\ominus} \right], \tag{15}$$

with phase angles $\varphi_j^\oplus = k(x_{j+1} - x_j)$ and $\varphi_j^\ominus = k(x_j - x_{j-1})$.

We will now revisit the conditions at channel head, vertex points and channel mouth and express these in terms of the unknown elevation amplitudes N_j , either directly or indirectly through the velocity amplitudes U_j^\oplus and U_j^\ominus and using Eqs. 14–15. Firstly, imposing the closed boundary condition at the channel head simply implies

$$U_{J+1}^\ominus = 0. \tag{16}$$

With the aid of Eq. 15, this effectively boils down to $N_{J+1} = N_J / \cos(k[l - x_J])$.

Secondly, Eq. 7, expressing continuity of mass at each vertex point, becomes

$$bh \left[U_j^\ominus - U_j^\oplus \right] = b_j h_j V_j = Y_j N_j, \tag{17}$$

for $j = 1, \dots, J$. The last equality herein shows that the mass transport through the entrance is proportional to the elevation amplitude, with the *basin admittance* Y_j as proportionality coefficient (Miles 1971; Garrett 1975; Lighthill 1978). The basin admittance thus equals the complex ratio of volume flux and elevation amplitudes at the entrance. This quantity depends on the secondary basin characteristics as well as the forcing frequency and follows from solving the corresponding model equations. To facilitate the solution and interpretation, it is convenient to represent the admittance in dimensionless form. We thus write

$$Y_j = \frac{i\omega b}{k} \tilde{Y}_j, \tag{18}$$

with dimensionless admittance \tilde{Y}_j given by

$$\tilde{Y}_j = \frac{A_j k}{b} \left[1 - \left(\frac{\gamma_j \omega}{\omega_{0,j}} \right)^2 \right]^{-1}. \tag{Helmholtz basin} \tag{19}$$

Here, we have used the frictional correction factor $\gamma_j = [1 - i r_j / (\omega h_j)]^{1/2}$, the eigenfrequency $\omega_{0,j} = [g b_j h_j / (A_j l_j)]^{1/2}$ (of the frictionless Helmholtz oscillator). A *subcritically forced* Helmholtz basin ($\omega < \omega_{0,j}$) has $\tilde{Y}_j > 0$ (in the absence of bottom friction) and is termed a *positive basin*. Conversely, a *supercritically forced* Helmholtz basin ($\omega > \omega_{0,j}$) has $\tilde{Y}_j < 0$ and is termed

a *negative basin*. Positive basins experience inflow (outflow) during rising (falling) tide at the entrance; for negative basins, the opposite is true. This terminology will be used later when presenting and interpreting the results (Sections 4 and 5).

Thirdly, we need to formulate a condition for the main channel mouth, where the elevations and mass transports on either side of $x = 0$ must match according to Eq. 2. As noted in Eq. 4, the elevation in the sea is the sum of the forcing wave and radiating wave, whereas the volume transport is entirely due to the radiating wave (the flow field of the forcing wave gives no transport through the mouth). The mouth conditions in Eq. 2 can thus be recast as

$$N_0 = N_{\text{forc}} + \langle N_{\text{rad}} \rangle, \tag{20}$$

$$bhU_0^\oplus = bh_s \langle U_{\text{rad}} \rangle = Y_{\text{rad}} \langle N_{\text{rad}} \rangle, \tag{21}$$

where the last equality shows that also the wave radiating into the sea satisfies an admittance relationship, now with *radiative admittance* Y_{rad} , again following from solving the model equations. Eliminating N_{rad} (and U_{rad}) from Eqs. 20–21 yields a single relationship involving N_0 , U_0^\oplus , and N_{forc} :

$$N_0 - Z_{\text{rad}} bhU_0^\oplus = N_{\text{forc}}, \tag{22}$$

where, instead of admittance, it is more convenient to use the *radiative impedance* $Z_{\text{rad}} = Y_{\text{rad}}^{-1}$. The radiative impedance, equal to the complex ratio of elevation and volume flux amplitudes, depends on sea geometry relative to channel geometry and on the forcing frequency. Analogous to the basin admittance, it is convenient to represent the impedance in dimensionless form, i.e.

$$Z_{\text{rad}} = \frac{k}{i\omega b} \tilde{Z}_{\text{rad}}, \tag{23}$$

with dimensionless radiative impedance \tilde{Z}_{rad} given by

$$\tilde{Z}_{\text{rad}} = \begin{cases} -i \frac{k_s}{k} \frac{k_s b}{2} \left(1 + \frac{2i}{\pi} \left[\frac{3}{2} - \Gamma - \log\left(\frac{1}{2} k_s b\right) \right] \right), & \text{(half-plane)} \\ -i \frac{k_s b}{k b_s} \left[1 + \sum_{m=1}^{\infty} \frac{2k_s}{v_m \xi_m} \sin^2 \xi_m \right], & \text{(semi-inf. strip)} \\ -i \frac{k_s}{k}, & \text{(channel extension)} \end{cases} \tag{24}$$

for the half-plane, semi-infinite strip and channel extension, respectively. In the upper expression (Buchwald 1971; Miles 1971; Garrett 1975), $\Gamma = 0.5772\dots$ is Euler’s constant. In the second expression, we use $\xi_m = m\pi b/b_s$ and v_m satisfying $v_m^2 = k_s^2 - (2m\pi/b_s)^2$ as well as $\Im\{v_m\} < 0$ (see Appendix C). The radiative impedance depends on the width ratio b_s/b and (through k_s/k) also on the depth ratio h_s/h . Based on the dependency of \tilde{Z}_{rad} on the depth ratio, as shown in Fig. 2 for the channel extension, we identify two limiting mouth conditions:

- The *deep sea limit*, characterised by $\tilde{Z}_{\text{rad}} = 0$, prescribes elevation at the channel mouth. It is obtained by letting $h_s/h \rightarrow \infty$ in any of the expressions in

¹The velocity amplitudes U_0^\ominus and U_{J+1}^\oplus are meaningless here as they refer to limits taken in regions outside the main channel.

Eq. 24, by which $k_s/k \downarrow 0$. As will be shown in Section 4, this limit is also well approximated by a wide sea with a depth identical to that of the main channel.

- The *channel extension of same depth (CESD) limit*, characterised by $\tilde{Z}_{rad} = -i$, prescribes the incoming wave (equivalent to Alebregtse et al. 2013). In this limit, both the width and depth of the sea and main channel are identical, i.e. $b_s = b$ and $h_s = h$ such that also $k_s = k$ in (the third expression of) Eq. 24.

The dependency of \tilde{Z}_{rad} on the ratio of sea width and channel width will be investigated in Section 4.2 and discussed in Section 5.2.

Finally, combining the conditions in Eqs. 16–17 and 22 with the vertex transport Eqs. 14–15 gives a set of linear equations, which is solved analytically. Here, we present the cases without secondary basin ($J = 0$) and with one or two secondary basins ($J = 1$ or $J = 2$) in matrix form:

$$\begin{bmatrix} 1 + \tilde{Z}_{rad}\tau_0^\oplus & -\tilde{Z}_{rad}\sigma_0^\oplus \\ -\sigma_1^\ominus & \tau_1^\ominus \end{bmatrix} \begin{bmatrix} N_0 \\ N_1 \end{bmatrix} = \begin{bmatrix} N_{forc} \\ 0 \end{bmatrix}, \tag{25}$$

$$\begin{bmatrix} 1 + \tilde{Z}_{rad}\tau_0^\oplus & -\tilde{Z}_{rad}\sigma_0^\oplus & 0 \\ -\sigma_1^\ominus & \tau_1^\oplus + \tau_1^\ominus - \tilde{Y}_1 & -\sigma_1^\oplus \\ 0 & -\sigma_2^\ominus & \tau_2^\ominus \end{bmatrix} \begin{bmatrix} N_0 \\ N_1 \\ N_2 \end{bmatrix} = \begin{bmatrix} N_{forc} \\ 0 \\ 0 \end{bmatrix}, \tag{26}$$

and

$$\begin{bmatrix} 1 + \tilde{Z}_{rad}\tau_0^\oplus & -\tilde{Z}_{rad}\sigma_0^\oplus & 0 & 0 \\ -\sigma_1^\ominus & \tau_1^\oplus + \tau_1^\ominus - \tilde{Y}_1 & -\sigma_1^\oplus & 0 \\ 0 & -\sigma_2^\ominus & \tau_2^\oplus + \tau_2^\ominus - \tilde{Y}_2 & -\sigma_2^\oplus \\ 0 & 0 & -\sigma_3^\ominus & \tau_3^\oplus \end{bmatrix} \begin{bmatrix} N_0 \\ N_1 \\ N_2 \\ N_3 \end{bmatrix} = \begin{bmatrix} N_{forc} \\ 0 \\ 0 \\ 0 \end{bmatrix}. \tag{27}$$

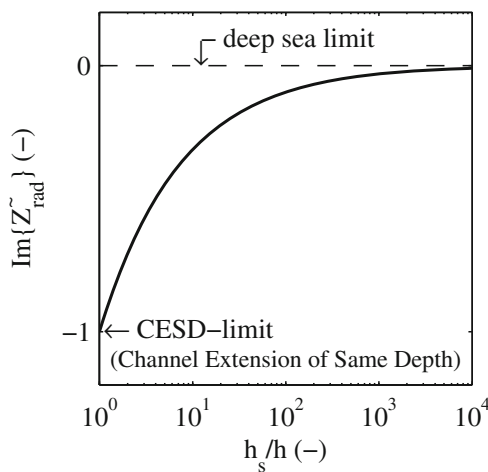


Fig. 2 Dependency of dimensionless radiative impedance \tilde{Z}_{rad} on the ratio h_s/h of sea depth and channel depth according to the third expression in Eq. 24, assuming no bottom friction. As $\Re\{\tilde{Z}_{rad}\} = 0$, only the imaginary part is plotted. The *dashed line* denotes the deep sea limit, the point $h_s/h = 1$ the so-called CESD-limit

Here, we have used the following shorthand notation: $\tau_j^\oplus = 1/\tan\varphi_j^\oplus$, $\tau_j^\ominus = 1/\tan\varphi_j^\ominus$, $\sigma_j^\oplus = 1/\sin\varphi_j^\oplus$ and $\sigma_j^\ominus = 1/\sin\varphi_j^\ominus$ with angles as defined below Eq. 15.

4 Results

4.1 Approach and reference parameter settings

We focus on the relative effect of the secondary basins compared to a reference situation without secondary basins. To present our results, we consider the elevation at the head of the main channel ($x = l$) and we define the complex amplification factor

$$A = N_{head}/N_{head}^{ref}. \tag{28}$$

The absolute value $|A|$ shows the so-called *amplitude gain*, its phase $\arg(A)$ the phase shift due to the presence of secondary basin. The reference value N_{head}^{ref} follows from solving Eq. 25, which gives, after applying trigonometric identities, the following result:

$$N_{head}^{ref} = \frac{N_{forc}}{\cos kl - \tilde{Z}_{rad} \sin kl}. \tag{29}$$

In the deep sea limit, this reduces to $N_{head} = N_{forc}/\cos kl$, whereas in the CESD-limit we obtain $N_{head} = N_{forc} \exp(-ikl)$.

To fully expose the dependencies of the amplification factor A , we vary the main channel length in the range $0 < l < l_{max}$ for parameter values taken from Table 1 (reference or alternative values). Basin position(s) will be varied in the range $0 < x_j < l$. In Sections 4.2 and 4.3, we present results without bottom friction ($r_s = r = r_j = 0$); the influence of bottom friction will be investigated in Section 5.4.

4.2 One secondary basin

The elevation amplitude at the head for a single secondary basin follows from solving Eq. 26, and we find

$$N_{head} = \frac{N_{forc}}{\cos kl - \tilde{Z}_{rad} \sin kl - \tilde{Y}_1 [\sin\varphi_1^\ominus + \tilde{Z}_{rad} \cos\varphi_1^\ominus] \cos\varphi_1^\oplus}. \tag{30}$$

In the deep sea limit, the amplification factor reduces to $A = [1 - \tilde{Y}_1 \sin\varphi_1^\ominus \cos\varphi_1^\oplus / \cos kl]^{-1}$. Alternatively, in the CESD-limit, we obtain $N_{head} = N_{forc}/[\exp(ikl) + i\tilde{Y}_1 \exp(i\varphi_1^\ominus) \cos\varphi_1^\oplus]$, such that $A = [1 + i\tilde{Y}_1 \cos\varphi_1^\oplus \exp(-i\varphi_1^\oplus)]^{-1}$. This last result reproduces the findings by Alebregtse et al. (2013). It depends on the distance $l - x_1$ from secondary basin

Table 1 Overview of model parameters, their reference values and alternative values

Description	Symbol	Reference value	Alternative values
Forcing amplitude	N_{forc}	0.5 m	
Angular frequency M2-tide	ω	$1.404 \times 10^{-4} \text{ rad s}^{-1}$	
Sea depth	h_s	10 m	
Sea width	b_s	10 km	1 km, 2 km, infinite
Main channel length (max. value in plots)	l_{max}	700 km	
Main channel depth	h	10 m	
Main channel width	b	1 km	
Helmholtz basin: basin area	A_j	20 km ²	10 km ² ('small'), 100 km ² ('large')
Helmholtz basin: channel length	l_j	1 km	2 km ('negative' basin)
Helmholtz basin: channel depth	h_j	5 m	1 m ('negative' basin)
Helmholtz basin: channel width	b_j	100 m	50 m ('negative' basin)
Helmholtz basin: eigenfrequency	$\omega_{0,j}$	$4.95 \times 10^{-4} \text{ rad s}^{-1}$	$7.00 \times 10^{-4} \text{ rad s}^{-1}$ ('small'), $2.21 \times 10^{-4} \text{ rad s}^{-1}$ ('large') $0.50 \times 10^{-4} \text{ rad s}^{-1}$ ('negative' basin)

to head only. Moreover, only if \tilde{Y}_1 is real and small ($|\tilde{Y}_1| \ll 1$), this further simplifies to $A \approx 1 - \frac{1}{2}\tilde{Y}_1 \sin 2\varphi_1^\oplus$, producing the specific alternating pattern of reduction and amplification already mentioned in the Introduction (Section 1).

For the reference parameter settings, Fig. 3 displays the situation without basin, with basin as well as the amplitude gain $|A|$ defined in Eq. 28. This is done for a range of main channel lengths l and for a range of secondary basin positions x_1 , which obviously must satisfy $x_1 < l$ thus

explaining the triangular plotting domain. To facilitate interpretation, l and x_1 have been scaled against the frictionless shallow water wavelength $\lambda = 2\pi/k_0 \approx 443 \text{ km}$. Figure 3a displays $|N_{\text{head}}/N_{\text{forc}}|$ according to Eq. 29, showing large amplification at $l/\lambda \approx \frac{1}{4}, \frac{3}{4}, \dots$. This is the well-known quarter wavelength resonance (and odd multiples of the quarter wavelength), here slightly modified due to radiative damping (e.g. Defant 1961). This pattern of straight tongues is independent of x_1 because there is no secondary basin. Figure 3b shows how the presence of a secondary

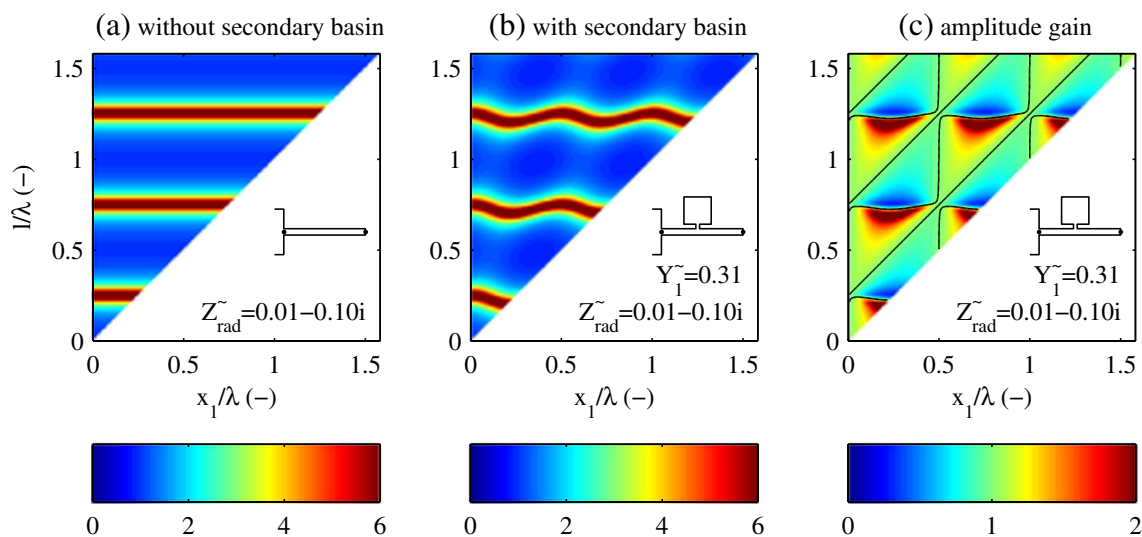


Fig. 3 Dimensionless elevation at channel head $|N_{\text{head}}/N_{\text{forc}}|$ for a situation (a) without secondary basin, (b) with one secondary basin at $x = x_1$. (c) amplitude gain $|A|$ (black lines denoting the unit contour). All quantities have been plotted as a function of basin position x_1 in

main channel (distance to mouth, which has no influence in case a) and main channel length l , both scaled against the frictionless shallow water wavelength $\lambda \approx 443 \text{ km}$. Parameter values in Table 1 (no bottom friction, $b_s = 10b$)

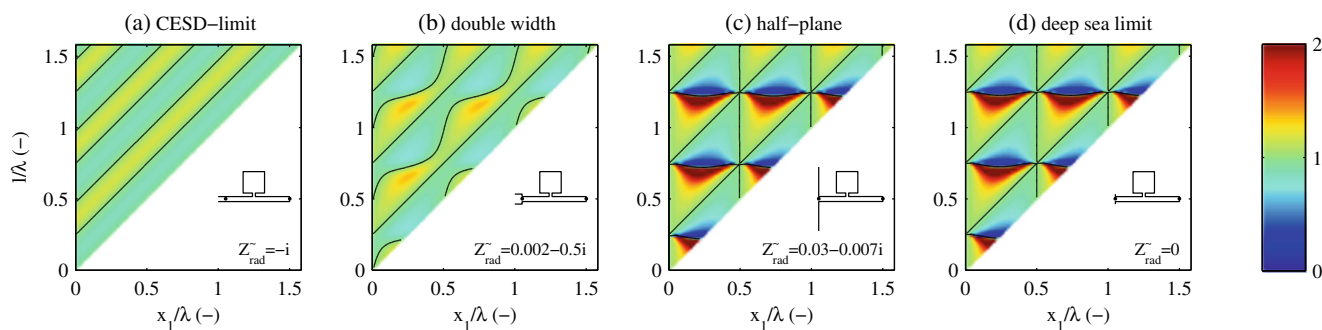


Fig. 4 Amplitude gain $|A|$ as in Fig. 3c, but now for a variety of sea configurations, all with $h_s = h$: **(a)** CESD-limit ($b_s = 1$ km), **(b)** sea with double width ($b_s = 2$ km), **(c)** half-plane ($b_s \rightarrow \infty$), **(d)** deep sea limit ($\tilde{Z}_{rad} = 0$, for which the sea width does not matter). Other parameters as in Table 1 (no friction)

basin turns the straight resonance tongues into a curly pattern, according to Eq. 30. In terms of the amplitude gain $|A|$ displayed in Fig. 3c, this leads to an intricate pattern of amplification and reduction as well as combinations of x and l that produce no change in elevation amplitude at the head ($|A| = 1$).

Figure 4 shows how the patterns of amplitude gain depend on sea geometry (see Table 1). We observe a smooth transition when gradually increasing the sea width b_s from the CESD-limit (Fig. 4a, with $|A|$ depending only on the distance $\delta = l - x_1$ to channel head) to the more pronounced pattern of the half-plane (Fig. 4c). Finally, the deep sea limit plotted in Fig. 4d turns out to be a good approximation of the amplitude gains for the reference case (Fig. 3c, with $b_s/b = 10$) and that of the half-plane.

Next, Fig. 5 shows how the patterns of amplitude gain change depend on the basin characteristics (see Table 1). The examples in Fig. 5a, b and c show how increasing the basin area A_j reduces the regions of amplification and intensifies the response. Increasing A_j further would turn the system from subcritically forced (‘positive’ basin, i.e. $\tilde{Y}_j > 0$) to supercritically forced (‘negative’ basin, i.e. $\tilde{Y}_j < 0$), for which the pattern of amplification and reduction roughly reverses. Another example of such a negative

basin is provided by Fig. 5d, here obtained for an inlet channel that is longer, shallower and narrower than the reference case (Table 1).

4.3 Two secondary basins

For a situation with two secondary basins, the elevation at the channel head is found to be

$$N_{head} = \frac{N_{forc}}{\cos kl - \tilde{Z}_{rad} \sin kl - f_1 \tilde{Y}_1 - f_2 \tilde{Y}_2 + f_{12} \tilde{Y}_1 \tilde{Y}_2}, \tag{31}$$

with coefficients given by

$$f_1 = [\sin \varphi_l - \tilde{Z}_{rad} \cos \varphi_l] \cos \varphi_{cr}, \tag{32}$$

$$f_2 = [\sin \varphi_{lc} - \tilde{Z}_{rad} \cos \varphi_{lc}] \cos \varphi_r, \tag{33}$$

$$f_{12} = [\sin \varphi_l + \tilde{Z}_{rad} \cos \varphi_l] \sin \varphi_c \cos \varphi_r. \tag{34}$$

Here, we have used the shorthand notation $\varphi_l = kx_1$, $\varphi_c = k[x_2 - x_1]$, $\varphi_r = k[l - x_2]$ as well as $\varphi_{lc} = \varphi_l + \varphi_c$ and $\varphi_{cr} = \varphi_c + \varphi_r$. The above result follows from applying trigonometric identities to the analytical solution of Eq. 27.

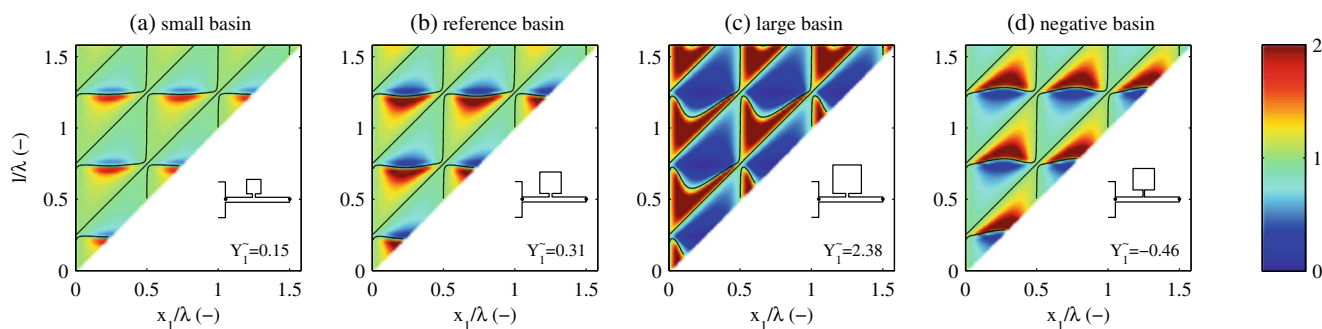
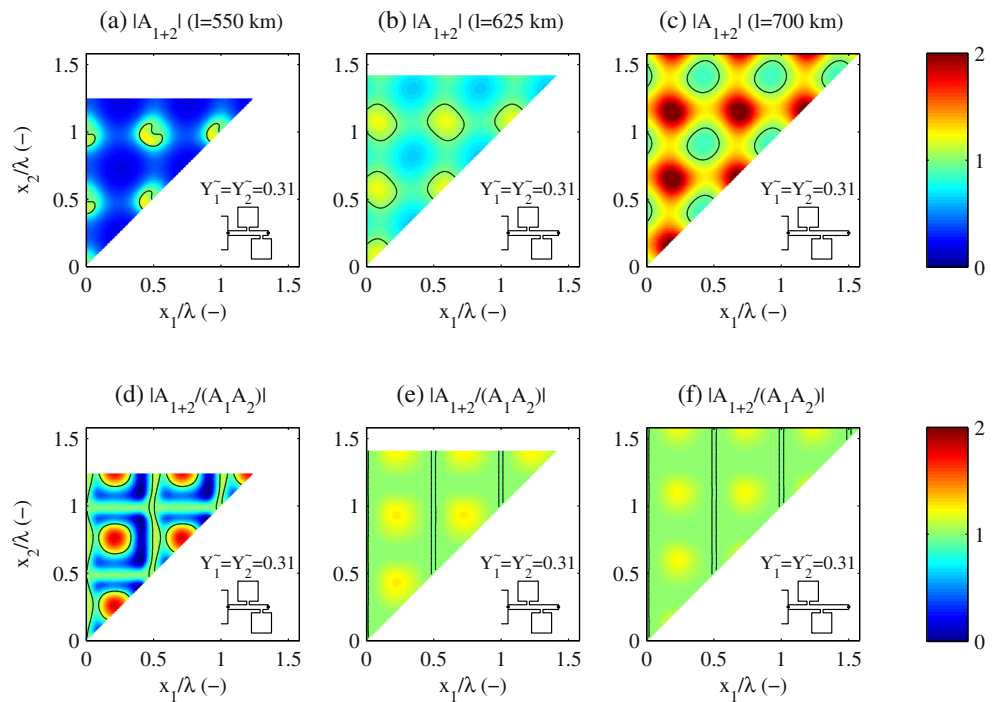


Fig. 5 Same as Fig. 4, but now for a variety of basin configurations: **(a)** small Helmholtz basin ($A_j = 10$ km²), **(b)** reference basin (same as Fig. 3c), **(c)** large basin ($A_j = 100$ km²), **(d)** example of a ‘negative’ basin ($l_j = 2$ km, $h_j = 1$ m, $b_j = 50$ m)

Fig. 6 Amplitude gain at channel head for a situation with two identical secondary basins, as a function of their positions x_1 and x_2 . The top row shows the amplitude gain $|A_{1+2}|$ according to Eq. 31 for different values of the main channel length l : (a) 550 km, (b) 625 km and (c) 700 km. The bottom row shows the corresponding ratio $Q = |A_{1+2}/(A_1 A_2)|$, showing an amplified (red shades) or weakened (blue) response compared to the separate effects. Black lines are the unit contours. The basin positions $x_{1,2}$ have been scaled against the frictionless shallow water wavelength $\lambda = 2\pi/k_0 \approx 443$ km. Parameter values as in Table 1



Particularly, one may wonder to what extent the amplitude gain from two secondary basins A_{1+2} , based on Eq. 31, differs from the product $A_1 A_2$ of the individual amplitude gains of the subbasins separately, as obtained earlier using Eq. 30 in Sections 4.2. To investigate this, we define the quantity $Q = |A_{1+2}/(A_1 A_2)|$. If $Q > 1$, the interaction between the basins leads to an amplified response compared to the response of two noninteracting basins; if $Q < 1$ the interaction leads to a weakened response. Both situations may occur. See Fig. 6, where this is illustrated for two identical retention basins and different values of the main channel length l .

To analyse this interaction further, we derive expressions for the amplitude gains A_{1+2} and $A_1 A_2$. Combining Eqs. 31 and 29 gives

$$A_{1+2} = \frac{1}{1 - \frac{f_1 \tilde{Y}_1 + f_2 \tilde{Y}_2}{\cos kl - \tilde{Z}_{\text{rad}} \sin kl} + \frac{f_{12} \tilde{Y}_1 \tilde{Y}_2}{\cos kl - \tilde{Z}_{\text{rad}} \sin kl}}, \tag{35}$$

whereas with the aid of Eq. 30 we obtain

$$A_1 A_2 = \frac{1}{1 - \frac{f_1 \tilde{Y}_1 + f_2 \tilde{Y}_2}{\cos kl - \tilde{Z}_{\text{rad}} \sin kl} + \frac{f_{12} \tilde{Y}_1 \tilde{Y}_2}{(\cos kl - \tilde{Z}_{\text{rad}} \sin kl)^2}}, \tag{36}$$

These results differ only regarding the so-called interaction term, i.e. in the third term in the denominator, which is proportional to $\tilde{Y}_1 \tilde{Y}_2$. Comparison of the third term in the denominators of Eqs. 35 and 36 shows that whether amplification ($Q > 1$), reduction ($Q < 1$) or no change ($Q = 1$) occurs, depends on the basins' locations and on channel

length. The analysis also shows that stronger interaction occurs for basins with larger dimensionless admittances, which is confirmed by other simulations not reported here.

5 Discussion

5.1 Physical mechanism

To unravel the physical mechanism, we will analyse the system's response to a single secondary basin at $x = x_1$, relative to the reference situation without basin. For clarity, we consider the case without bottom friction (see Fig. 7). This reference case is a standing wave in the main channel producing an elevation amplitude N_1^{ref} at $x = x_1$ (Fig. 7a) that can be assumed to be real-valued and positive.²

If $N_1^{\text{ref}} \neq 0$, adding the secondary basin triggers oscillations inside the secondary basin as well as an oscillatory volume transport through the entrance. To accommodate this transport, additional waves must develop in the main channel on either side of the inlet (while respecting the conditions at the vertex point as well as channel mouth and head). This is accompanied by a yet unknown change in elevation amplitude N'_1 at $x = x_1$ (see Fig. 7b, c), which will also affect the amplitude at the channel head. From Eq. 17, the matching of volume fluxes at the vertex point can be

²This can be assumed without loss of generality (by a suitable definition of the moment $t = 0$).

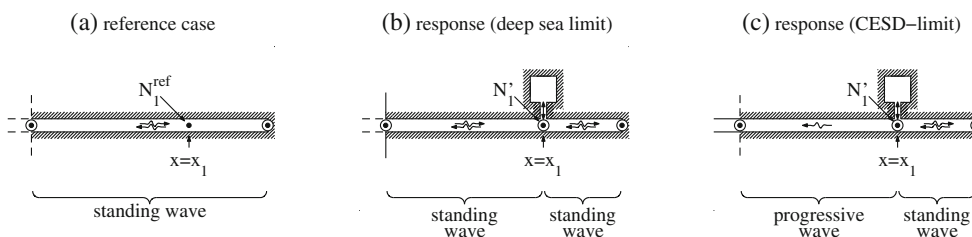


Fig. 7 Sketch of the physical mechanism for two limiting sea geometries. The solution is the superposition of (a) the standing wave in the reference case without basin and the response to the secondary basin. This response consists of a standing wave at the landward side and a

wave on the seaward side of $x = x_1$. For the limiting sea geometries, the latter is either (b) a standing wave (deep sea limit) or (c) a seaward progressive wave (CESD-limit)

written as

$$(Y_{seaw} - Y_{landw})N'_1 = Y_1(N_1^{ref} + N'_1), \tag{37}$$

where we have introduced landward and seaward channel admittances Y_{landw} and Y_{seaw} , respectively.

Just like the reference case, the additional landward wave is a standing wave with an elevation antinode at $x = l$, corresponding to a dimensionless admittance $\tilde{Y}_{landw} = \tan \varphi_1^\oplus$ (Appendix D, Fig. 7b, c). Analogous to the definition of positive and negative basins in Section 3, a positive \tilde{Y}_{landw} -value physically means inflow into the landward end during rising tide at the vertex point (a negative value implying the opposite). Because the seaward admittance depends on sea geometry relative to channel geometry, we will now analyse the additional seaward wave for the two limiting mouth conditions introduced earlier in Section 3.

- For the deep sea limit, the additional seaward wave is a standing wave with an elevation node at the mouth (Fig. 7b), for which the dimensionless admittance reads $\tilde{Y}_{seaw} = 1/\tan \varphi_1^\ominus$ (Appendix D). A positive \tilde{Y}_{seaw} -value physically means outflow from the seaward end during rising tide at the vertex point (a negative value implying the opposite).
- For the CESD-limit, the additional seaward wave is an outgoing progressive wave (Fig. 7c), for which $\tilde{Y}_{seaw} = i$ (Appendix D).

Equation (37) can be solved to obtain

$$\frac{N'_1}{N_1^{ref}} = \frac{1}{(\tilde{Y}_{seaw} - \tilde{Y}_{landw})/\tilde{Y}_1 - 1}, \tag{38}$$

now expressed in terms of dimensionless admittances. Hence, it is the imbalance between \tilde{Y}_{seaw} and \tilde{Y}_{landw} , that, along with \tilde{Y}_1 , controls the response. Amplification at the vertex point and hence also at the channel head occurs if $|N_1^{ref} + N'_1| > N_1^{ref}$, reduction if $|N_1^{ref} + N'_1| < N_1^{ref}$. Alternatively, there are three distinct cases in which no change occurs, i.e. $|N_1^{ref} + N'_1| = N_1^{ref}$. Here, we will analyse them for each of the two limiting mouth conditions (Fig. 8).

- Case I: The reference standing wave has a node at $x = x_1$, i.e. $N_1^{ref} = 0$. This leaves the secondary basin unforced. This case, independent of sea geometry, is denoted with the blue diagonal lines in Fig. 8.
- Case II: The additional waves are such that only a phase shift occurs at $x = x_1$ and, hence, also at the channel head. For the deep sea limit, this occurs if $N'_1/N_1^{ref} = -2$, implying a 180° phase shift. For $\tilde{Y}_1 \ll 1$ implies $\cos kl \approx 0$ and hence $l/\lambda \approx \frac{1}{4}, \frac{3}{4}, \dots$, denoted by the red curly lines in Fig. 8a. In the CESD-limit, this case $\tan \varphi_1^\oplus = -\frac{1}{2}\tilde{Y}_1$ and the phase shift depends on \tilde{Y}_1 . For small basins, this reduces to the situation already described by Alebregtse et al. (2013): $\tan \varphi_1^\oplus = 0$, i.e. $[l - x_1]/\lambda = \frac{1}{2}, 1, \frac{3}{2}$, and so on. These conditions are indicated by the red diagonal lines in Fig. 8b.
- Case III: The additional seaward wave had a node at $x = x_1$, i.e. $N'_1 = 0$. Its volume transport is then sufficient to accommodate the oscillations in the secondary basin, without triggering an additional wave at the landward side. This occurs if $\tilde{Y}_{seaw} = 1/\tan \varphi_1^\ominus \rightarrow \infty$, i.e. if $x_1/l = \frac{1}{2}, 1, \frac{3}{2}$, and so on, as shown by the green vertical lines in Fig. 8a. Case III is not possible in the CESD-limit.

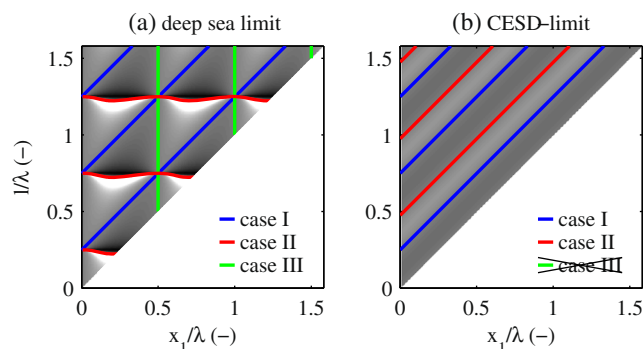


Fig. 8 Cases in which no amplitude change, for the two limiting mouth conditions: (a) deep sea limit, (b) CESD-limit. The cases are sketched as coloured ($|A|=1$)-contours in grey-shade copies of Fig. 4a and d. For an explanation of case I (blue contours), case II (red) and case III (green), see main text

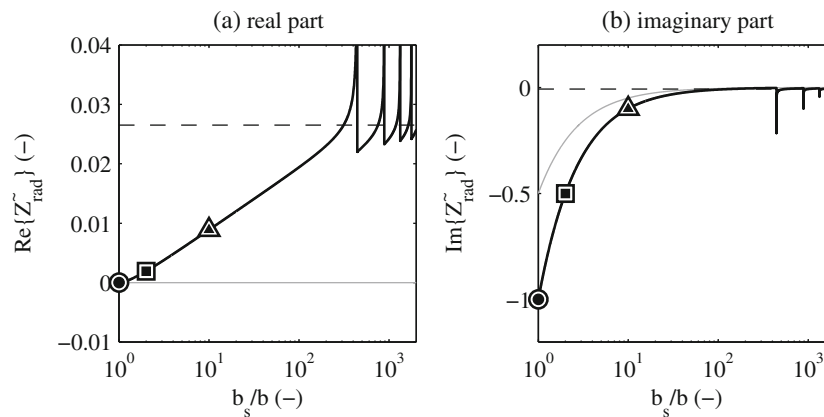


Fig. 9 Dependency of dimensionless radiative impedance \tilde{Z}_{rad} on the ratio b_s/b of sea width and channel width according to the second expression in Eq. 24: **a** real part, **b** imaginary part. The symbols represent three cases depicted in Section 4: channel extension (circle, Fig. 4a), double width (square, Fig. 4b) and the reference case

(triangle, Fig. 3). The *dashed line* indicates the half plane (Fig. 4c). Parameter values as in Table 1 (except b_s which is varied, no bottom friction, $k_s b = 0.0142$). The *grey solid lines* denote \tilde{Z}_{rad} of the model by Zimmerman (1992) according to Eq. 39

For small secondary basins, i.e. for basins with $|\tilde{Y}_1| \ll 1$, the last term on the right-hand side of Eq. 37 is negligible. The influence of the elevation change N'_1 on the transport into and out of the basin, i.e. the contribution of N'_1 on the right-hand side of Eq. 7, is then a higher order effect that can be neglected. For larger secondary basins, this can no longer be neglected. Increasing the value of $|\tilde{Y}_1|$ to a sufficiently large value will turn situations where amplification occurs into a situation with amplitude reduction, because the additional mass transport (due to N'_1) is then so large that it can no longer be accommodated by the difference in transport across the vertex point in the main channel. As a result, the sign of N'_1/N_1 changes. Hence, large secondary basins are generally more likely to produce amplitude reduction than small basins. This is apparent from the amplification regions in Fig. 5a, b and c.

5.2 Sea geometry

The dimensionless *radiative impedance* \tilde{Z}_{rad} introduced in Eqs. 22–24 is the key parameter through which the sea geometry enters our analysis. Our model results show a smooth transition between the CESD-limit and the deep sea limit (see Fig. 4). To further clarify this, Fig. 9 shows how the radiative impedance \tilde{Z}_{rad} depends on the width ratio b_s/b . Particularly, increasing b_s/b from 1, the radiative impedance quickly approaches the value of the half-plane limit ($b_s/b \rightarrow \infty$), which in turn strongly resembles the deep sea limit. This result was obtained for $h_s = h$; if the sea is deeper than the main channel, the mouth condition will be even closer to that of the deep sea limit.

The asymptotes showing up in Fig. 9 for certain values of b_s/b are associated with a transverse resonance

phenomenon. These peaks occur when the sea width is a multiple of the shallow water wavelength,³ i.e. if $b_s = m\lambda_s$. One of the normal modes then has a longitudinal wave number equal to zero ($\nu_m = 0$ in the terminology of Appendix C); it is then on the border between being free (propagating in the negative x -direction) and being bound (exponentially decaying in the negative x -direction). Increasing bottom friction causes these peaks to damp.

Including Coriolis effects in our model would make the forcing at sea more realistic, producing a Kelvin wave propagating along the coast. However, as the forcing acts only at a single point on the main channel, the spatial pattern of the forcing wave in itself is not relevant. What is relevant is the way in which sea geometry affects the radiating wave and hence the radiative impedance. Coriolis effects only have a minor effect on the radiative sea impedance (Garrett 1975).

As an alternative to the semi-infinite strip depicted in Fig. 1, the sea geometry can also be represented as an infinite channel of width b_s , stretching to $+\infty$ and $-\infty$ in the y -direction, i.e. perpendicular to the main channel (Zimmerman 1992). The forcing wave would then be a progressive tidal wave, propagating in the positive or negative y -direction. Adopting a cross-sectionally averaged approach also in the sea, the corresponding dimensionless radiative impedance is given by

$$\tilde{Z}_{\text{rad}} = \frac{-ik_s b}{2kb_s}. \quad (\text{model by Zimmerman 1992}) \quad (39)$$

³In addition to these *even* multiples of *half* the wavelength $\frac{1}{2}\lambda_s$, also *odd* multiples may cause resonant peaks. However, the symmetric position of the channel mouth prevents these odd modes from appearing here.

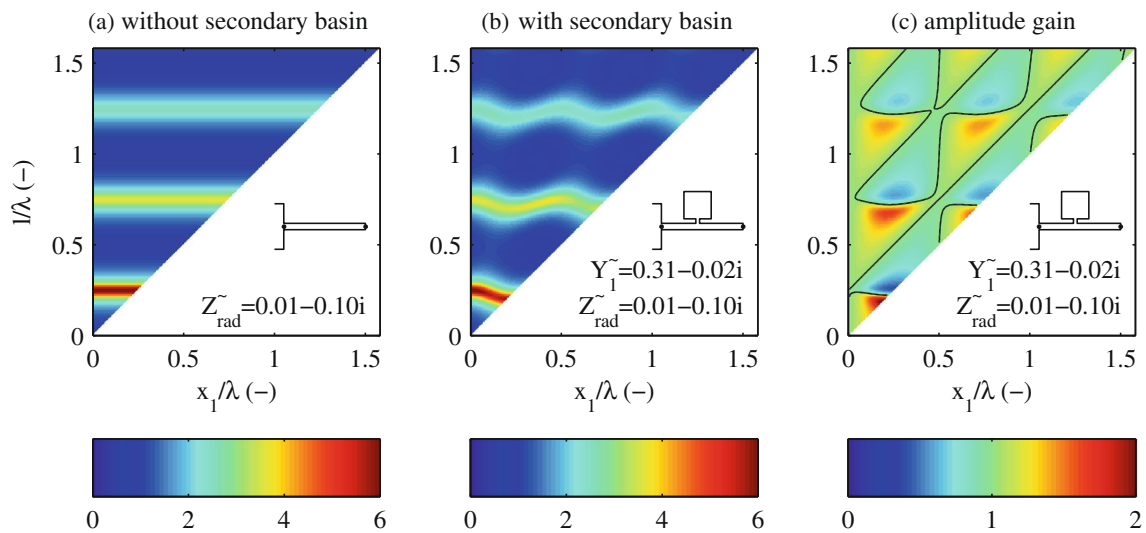


Fig. 10 Same as Fig. 3, but now for moderate friction

This result resembles that for the channel extension in the third expression of Eq. 24, except for the factors $\frac{1}{2}$ and b/b_s , accounting for the two directions in which the channel stretches and the difference in width, respectively. The width-dependency of Eq. 39 is plotted using grey lines in Fig. 9.

5.3 Basin characteristics

The dimensionless *basin admittance* \tilde{Y}_j introduced in Eqs. 17–19 is the key parameter through which the basin characteristics enter our analysis. This can for example be seen from the matrix systems Eq. 26 and the solutions in Eqs. 30–31. For Helmholtz basins, \tilde{Y}_j was found to depend on the geometry of the basin (surface area) and inlet channel (length, depth, width and friction coefficient), relative to that of the main channel (width, depth and friction coefficient), as well as forcing frequency. On the basis of \tilde{Y}_j , we have made a distinction into small basins ($|\tilde{Y}_j| \ll 1$) and basins that are not small. Only for small basins in the CESD-limit, the pattern obtained by Alebregtse et al. (2013) is obtained. For larger $|\tilde{Y}_j|$ -values, the pattern is distorted. In general, larger $|\tilde{Y}_j|$ -values imply stronger interactions, in the case of multiple basins. In the frictionless case, we have furthermore seen that subcritically forced Helmholtz basins act as positive basins ($\tilde{Y}_j > 0$) and that supercritically forced Helmholtz basins act as negative basins ($\tilde{Y}_j < 0$, for which the amplification/reduction pattern roughly reverses).

Importantly, our approach is not restricted to Helmholtz basins. Instead, one may for example consider a linear channel, characterised by its length l_j , width b_j , depth h_j and friction coefficient r_j . As derived in Appendix E, the

dimensionless basin admittance is given by

$$\tilde{Y}_j = \frac{kb_j}{k_j b} \tan k_j l_j, \quad (\text{linear channel}) \quad (40)$$

where $k_j = \gamma_j \omega / \sqrt{gh_j}$ is the shallow water wave number, with frictional correction factor γ_j as defined earlier below Eq. 19. This result is identical to the ‘secondary channel factor’ used by Alebregtse et al. (2013). According to Eq. 40, also linear channels can be classified as small or not small, and (for the case without bottom friction) as positive or negative. They are positive if $l_j < \frac{1}{4}\lambda$, negative if $\frac{1}{4}\lambda < l_j < \frac{1}{2}\lambda$, positive again if $\frac{1}{2}\lambda < l_j < \frac{3}{4}\lambda$ and so on ($\lambda_j = 2\pi/k_j$ being the shallow water wavelength in the linear channel).

Alternatively, the value of \tilde{Y}_j can also be derived from a separate model, e.g. in the case of basins with a more complex geometry. A prerequisite is that this separate model is also linear such that the linear admittance relationship in Eq. 17 can indeed be applied.

Finally, we note that this study, focused on tidally forced systems, can also be applied to investigate the resonance characteristics of harbours forced by, e.g., long gravity waves.

5.4 Role of bottom friction

So far, results have been presented without bottom friction. Figure 10 shows the amplitude gain patterns in Fig. 3 change, if we set the friction coefficients to one-tenth of the values presented in Appendix A. Dissipation of the wave damps the amplitudes, more strongly for larger values of the channel length (Fig. 10a, b). The amplitude

gain thus becomes closer to unity and also the pattern looks different (Fig. 10c). Even higher friction leads to a more strongly damped pattern. Including channel (width) convergence, neglected in our study, would provide a mechanism that counteracts the damping due to bottom friction.

Finally, we remark that including bottom friction distorts the physical mechanisms presented in Section 5.1, making the distinction between cases I, II, and III less apparent (see contours in Fig. 10c).

6 Conclusions

We have developed an idealised model study of tidal dynamics in channels with multiple secondary basins and investigated the effect of one or two basins on the tidal elevation amplitude at the channel head. The amplitude gain, which may imply amplification, reduction or no change, is found to depend on the geometries of sea and channel, the type/geometry and position of the secondary basin and bottom friction.

Sea geometry affects the way radiative damping manifests itself and thus controls the conditions that effectively apply at the main channel mouth. This is reflected in the dimensionless *radiative impedance* \tilde{Z}_{rad} , ranging from one extreme of prescribing the incoming tidal wave (sea represented as a channel extension of same depth) to the other extreme of prescribing the elevation (deep sea). In these limits, the physical mechanisms underlying the response are fundamentally different. Channel geometry matters as it controls the proximity to resonance, and secondary basins may bring the system closer to resonance or further away from it.

Next, the role of the secondary basin is contained in its position as well as in the dimensionless *basin admittance* \tilde{Y}_j , which inspires two classifications: (i) between positive and negative secondary basins, depending on whether — in the frictionless case — they attract or release water during rising tide at the entrance (positive implying $\tilde{Y}_j > 0$, negative $\tilde{Y}_j < 0$); (ii) between basins that are small ($|\tilde{Y}_j| \ll 1$) and basins that are not small. Secondary basins of this last class may interact such as to significantly amplify or weaken their individual responses. Moreover, the position of the basin is important. Because of the general mouth conditions not only the distance to the head matters (as in the extended channel case), but now also the distance to mouth matters.

Bottom friction modifies each of the above aspects, generally leading to dampened response. We expect that including channel (width) convergence, as observed in, e.g., the Ems Estuary and Western Scheldt, will affect the response patterns only quantitatively.

Acknowledgments This work is part of the research programme NWO-ALW project 843.10.005, which is financed by the Netherlands Organisation for Scientific Research (NWO) and the Chinese Organisation for Scientific Research (NSFC).

We thank Ronald Brouwer and two anonymous reviewers for their comments on the manuscript.

Open Access This article is distributed under the terms of the Creative Commons Attribution License which permits any use, distribution, and reproduction in any medium, provided the original author(s) and the source are credited.

Appendix A: Friction coefficients from Lorentz' linearisation

We use Lorentz' linearisation (Lorentz 1922; Zimmerman 1982) to determine the values of the friction coefficients in Eqs. 1 and 6, i.e.

$$r = \frac{8c_d\hat{u}}{3\pi}, \quad r_j = \frac{8c_d\hat{v}_j}{3\pi}. \quad (41)$$

Apart from a drag coefficient $c_d = 2.5 \times 10^{-3}$, this involves typical scales \hat{u} and \hat{v}_j for the velocities in main channel and secondary basins, respectively, which require further specification.

For the main channel, we let \hat{u} be equal to the velocity amplitude of a frictionless shallow water wave of elevation amplitude N_{forc} . For the secondary basins represented as Helmholtz basins, we take the channel velocity amplitude if it were frictionless and forced by an elevation amplitude N_{forc} . The above considerations lead to

$$\hat{u} = N_{\text{forc}}\sqrt{g/h}, \quad \hat{v}_j = \frac{g\omega N_{\text{forc}}}{\ell_j|\omega^2 - \omega_{0,j}^2|}, \quad (42)$$

with eigenfrequency $\omega_{0,j} = [gb_jh_j/(A_j\ell_j)]^{1/2}$. More complicated approaches, such as an iterative approach to determine the velocity scales (e.g., Roos and Schutte-laars 2011), are beyond the scope of this study.

Appendix B: Model equations in sea region

In the sea region, conservation of momentum and mass is expressed by the two-dimensional shallow water equations in including bottom friction:

$$\frac{\partial u_s}{\partial t} + \frac{r_s u_s}{h_s} = -g \frac{\partial \eta_s}{\partial x}, \quad (43)$$

$$\frac{\partial v_s}{\partial t} + \frac{r_s v_s}{h_s} = -g \frac{\partial \eta_s}{\partial y}, \quad (44)$$

$$\frac{\partial \eta_s}{\partial t} + h_s \left[\frac{\partial u_s}{\partial x} + \frac{\partial v_s}{\partial y} \right] = 0. \quad (45)$$

Here, r_s is a friction coefficient. Analogous to Appendix A, we use $r_s = 8c_d \hat{u}_s / (3\pi)$ with $\hat{u}_s = N_{\text{forc}} \sqrt{g/h_s}$. Boundary conditions require zero normal flow at the closed sea boundaries, as well as an incoming wave from the left and matching of elevation and transport across the channel mouth.

Appendix C: Radiative impedance for sea as semi-infinite strip

Let us consider the problem of depth-averaged flow in a semi-infinite strip of width b_s , defined by the domain $\Omega = \{(x, y) \mid x < 0, |y| < \frac{1}{2}b_s\}$. Model equations are as specified in Appendix B. The problem for the radiating wave is forced by a spatially uniform⁴ flow U_{rad} at the channel mouth (in the positive x -direction), i.e. at $x = 0$ and for $|y| < \frac{1}{2}b$. The complex amplitude of the along-basin flow of the radiative wave is given by

$$U_{\text{rad}}(x, y) = \langle U_{\text{rad}} \rangle \frac{b}{b_s} \left[\exp(ik_s x) + \sum_{m=1}^{\infty} \frac{2 \sin \xi_m}{\xi_m} \times \exp(i\nu_m x) \cos\left(\frac{2\xi_m y}{b}\right) \right], \quad (46)$$

with $\xi_m = m\pi b/b_s$ and wave number ν_m , satisfying $\nu_m^2 = k_s^2 - (2m\pi/b_s)^2$ and $\Im\{\nu_m\} < 0$. The elevation pattern follows from applying the along-basin momentum equation, i.e. from using $i\omega\gamma^2 U_{\text{rad},s} = -g \frac{\partial N_{\text{rad},s}}{\partial x}$. The complex amplitude of the surface elevation thus becomes

$$N_{\text{rad}}(x, y) = \frac{-h_s k_s b \langle U_{\text{rad}} \rangle}{\omega b_s} \left[\exp(ik_s x) + \sum_{m=1}^{\infty} \frac{2k_s \sin \xi_m}{\nu_m \xi_m} \times \exp(i\nu_m x) \cos\left(\frac{2\xi_m y}{b}\right) \right]. \quad (47)$$

Averaging this last expression over the channel mouth gives

$$\langle N_{\text{rad}} \rangle = \frac{-h_s k_s b \langle U_{\text{rad}} \rangle}{\omega b_s} \left[1 + \sum_{m=1}^{\infty} \frac{2k_s \sin^2 \xi_m}{\nu_m \xi_m^2} \right], \quad (48)$$

which is equivalent to the admittance relationship in Eq. 21 and the second expression in Eq. 24.

Appendix D: Landward and seaward admittances in the main channel

Here, we will derive the channel admittances used in Section 5.1. To this end, we define the complex amplitudes N' and U' of surface elevation and channel velocity, respectively, both corresponding to the additional waves emerging

⁴According to Miles (1971), the impedance is insensitive to the shape of the cross-channel velocity profile.

in response to the secondary basin. The standing wave at the landward side of the vertex point satisfies

$$N'_{\text{landw}}(x) = N'_1 \frac{\cos(k[x - l])}{\cos \varphi_1^{\oplus}}, \quad (49)$$

$$U'_{\text{landw}}(x) = -\frac{iN'_1}{\gamma} \sqrt{\frac{g}{h}} \frac{\sin(k[x - l])}{\cos \varphi_1^{\oplus}}, \quad (50)$$

such that, analogous to Eq. 17 and using Eq. 18, $\tilde{Y}'_{\text{landw}} = \tan \varphi_1^{\oplus}$.

For the deep sea limit, the wave on the seaward side is also a standing wave. However, because the mouth condition permits no elevation change, it must have an elevation node at $x = 0$:

$$N'_{\text{seaw}}(x) = N'_1 \frac{\sin kx}{\sin \varphi_1^{\ominus}}, \quad (51)$$

$$U'_{\text{seaw}}(x) = \frac{iN'_1}{\gamma} \sqrt{\frac{g}{h}} \frac{\cos kx}{\sin \varphi_1^{\ominus}}, \quad (52)$$

such that $\tilde{Y}'_{\text{seaw}} = 1/\tan \varphi_1^{\ominus}$.

Alternatively, in the CESD-limit, the wave on the seaward side is not a standing wave but a wave propagating toward the mouth. Equations 51–52 must then be replaced with

$$N'_{\text{seaw}}(x) = N'_1 \exp(ik[x - x_1]), \quad (53)$$

$$U'_{\text{seaw}}(x) = -\frac{N'_1}{\gamma} \sqrt{\frac{g}{h}} \exp(ik[x - x_1]). \quad (54)$$

giving $\tilde{Y}'_{\text{seaw}} = i$.

Appendix E: Admittance of a linear secondary channel

A linear prismatic channels is characterised by its length l_j , width b_j and depth h_j . Unknowns are the cross-sectionally averaged channel velocity $v_j(y, t)$, positive when pointing into the channel and surface elevation $\beta_j(y, t)$, both functions of the along-channel coordinate y and time t , and satisfying conservation laws similar to those for the main channel in Eq. 1. We thus write

$$\frac{\partial v_j}{\partial t} + \frac{r_j v_j}{h_j} = -g \frac{\partial \beta_j}{\partial y}, \quad \frac{\partial \beta_j}{\partial t} + h_j \frac{\partial v_j}{\partial y} = 0. \quad (55)$$

Analogous to the description of the main channel in Appendix A, we introduce a linear friction coefficient $r_j = 8c_d \hat{v}_j$ with velocity scale $\hat{v}_j = N_{\text{forc}} \sqrt{g/h_j}$. Boundary conditions require matching of elevation at mouth ($\beta_j = \eta_j$ at $y = 0$) and zero flow at the closed end ($v = 0$ at $y = l_j$).

Analogous to Eqs. 8–9, we define $\beta_j(y, t) = \Re \{B_j(y) \exp(i\omega t)\}$ and $v_j(y, t) = \Re \{V_j(y) \exp(i\omega t)\}$,

with complex elevation and velocity amplitudes $B_j(y)$ and $V_j(y)$, respectively. These amplitudes are given by

$$V_j(y) = -\frac{iN_j}{\gamma_j} \sqrt{\frac{g}{h_j}} \frac{\sin(k_j[x - l_j])}{\cos k_j l_j}, \quad B_j(y) = N_j \frac{\cos(k_j[y - l_j])}{\cos k_j l_j}, \quad (56)$$

where $k_j = \gamma_j \omega / \sqrt{gh_j}$ is the shallow water wave number, with frictional correction factor γ_j as defined earlier below Eq. 19. The (dimensional) basin admittance thus becomes

$$Y_j = \frac{b_j h_j V_j(0)}{N_j} = \frac{ib_j \omega}{k_j} \tan k_j l_j, \quad (57)$$

giving the dimensionless admittance \tilde{Y}_j as presented in Eq. 40.

References

- Alebregtse NC, de Swart HE (2014) Effect of a secondary channel on the non-linear tidal dynamics in a semi-enclosed channel: a simple model. *Ocean Dyn* 64(4):573–585. doi:[10.1007/s10236-014-0690-0](https://doi.org/10.1007/s10236-014-0690-0)
- Alebregtse NC, de Swart HE, Schuttelaars HM (2013) Resonance characteristics of tides in branching channels. *J Fluid Mech* 728:R3. doi:[10.1017/jfm.2013.319](https://doi.org/10.1017/jfm.2013.319)
- Buchwald VT (1971) The diffraction of tides by a narrow channel. *J Fluid Mech* 46(3):501–511. doi:[10.1017/S0022112071000661](https://doi.org/10.1017/S0022112071000661)
- Defant A (1961) *Physical oceanography*. Pergamon Press
- Donner M, Ladage F, Stoschek O (2012) Impact and retention potential of tidal polders in an estuary with high suspended sediment concentrations. In: *Proceedings of 10th International Conference on Hydrosience & Engineering (ICHE)*, Orlando, Florida., University of Central Florida
- Garrett C (1975) Tides in gulfs. *Deep-Sea Res* 22(1):23–35. doi:[10.1016/0011-7471\(75\)90015-7](https://doi.org/10.1016/0011-7471(75)90015-7)
- Lighthill J (1978) *Waves in fluids*. Cambridge University Press
- Lorentz HA (1922) Het in rekening brengen van den weerstand bij schommelende vloeistofbewegingen. *De Ingenieur* 37:695. in Dutch
- Miles JW (1971) Resonant response of harbours: an equivalent-circuit analysis. *J Fluid Mech* 46(2):241–265. doi:[10.1017/S002211207100051X](https://doi.org/10.1017/S002211207100051X)
- Roos PC, Schuttelaars HM (2011) Influence of topography on tide propagation and amplification in semi-enclosed basins. *Ocean Dyn* 61(1):21–38. doi:[10.1007/s10236-010-0340-0](https://doi.org/10.1007/s10236-010-0340-0)
- Stronkhorst J, Mulder J (2014) Considerations on managed realignment in The Netherlands. In: *Managed realignment: a viable long-term coastal management strategy?*, SpringerBriefs in Environmental Science, Springer Netherlands, pp 61–68. doi:[10.1007/978-94-017-9029-1_5](https://doi.org/10.1007/978-94-017-9029-1_5)
- Zimmerman JTF (1982) On the Lorentz linearization of a quadratically damped forced oscillator, vol 89
- Zimmerman JTF (1992) On the Lorentz linearization of a nonlinearly damped tidal Helmholtz oscillator. *Proc Kon Ned Akad Wetensch* 95:127–145